Linear and Nonlinear Stability Analysis of a Three-Dimensional Boundary Layer over a Hump

Westerbeek, S.H.J.; Sumariva, Juan Alberto Franco ; Michelis, T.; Hein, Stefan; Kotsonis, M.

DOI
10.2514/6.2023-0678

Publication date
2023

Document Version
Final published version

Published in
AIAA SciTech Forum 2023

AIAA SciTech Forum
23-27 January 2023, National Harbor, MD & Online
AIAA SCITECH 2023 Forum

10.2514/6.2023-0678

Linear and Nonlinear Stability Analysis of a Three-Dimensional Boundary Layer over a Hump

S. Westerbeek*, T. Michelis†, M. Kotsonis‡
Delft University of Technology, Section of Aerodynamics, Leeghwaterstraat 42, 2628CA Delft, The Netherlands,

J.A. Franco§, S. Hein¶
German Aerospace Center, Institute of Aerodynamics and Flow Technology, Bunsenstrasse 10, 37073 Göttingen, Germany

The Parabolized Stability Equations (PSE), Adaptive Harmonic Linearized Navier-Stokes (AHLNS) and Harmonic Navier-Stokes (HNS) solvers are used to analyze the linear and nonlinear stability of swept-wing boundary layers under the influence of smooth wall deformations of varying size and geometry. Special attention is given to the validity of the slowly varying flow assumption of PSE via a comparison with AHLNS and HNS results. The surface deformations analyzed in this work are found to affect the development of the primary stationary crossflow instability mode as well as higher harmonics. Analysis of the locally most amplified mode reveals successive modulation of the growth rate in the vicinity of the surface deformation. This process was found to be largely governed by linear terms and driven by the base flow modification due to the deformed wall. Similarly, the base flow modification causes higher harmonics to experience a significant destabilization. This is followed by stabilization as nonlinear interactions become dominant. The PSE methodology proved capable of predicting the stability response for small wall deformations with only minor amplitude discrepancies compared to HNS results. The main difference was found to occur in the wall-normal velocity profiles of the mean flow distortion mode. The deviations of the PSE results compared to harmonic stability methods increased as the protuberance was made steeper. Moreover, the PSE framework was not able to converge for all cases nonlinearly.

I. Nomenclature

x, ξ	=	Streamwise coordinate (global and body-fitted resp.)
y, η	=	Wall-normal coordinate (global and body-fitted resp.)
z	=	Spanwise coordinate (global and body-fitted resp.)
U, u'	=	Streamwise velocity (base and perturbation resp.)
V, v'	=	Wall-normal velocity (base and perturbation resp.)
W, w'	=	Spanwise velocity (base and perturbation resp.)
P, p'	=	Static pressure (base and perturbation resp.)
$\mathbf{Q}, \mathbf{q}'$	=	State vector of velocities and pressure
α	=	Streamwise wavenumber
β	=	Spanwise wavenumber
ω	=	Angular frequency
A	=	Maximum streamwise perturbation velocity
δ_{99}	=	Boundary layer height based on U
i	=	Imaginary unit
h	=	Protuberance height
b	=	Protuberance width
x_c	=	Protuberance center location
$_0$	=	Inflow value
$'$	=	Perturbation value
$\bar{}$	=	Dimensional quantity
*	=	Integration quantity
ν	=	Kinematic viscosity
$\bar{\delta}_0$	=	δ_{99} at the inflow, characteristic length
Re	=	$\frac{\bar{U}_0 \cdot \bar{\delta}_0}{\bar{\nu}}$ Reynolds number

*Ph.D. Candidate, Department of Flow Physics and Technology, S.H.J.Westerbeek@tudelft.nl
†Post-Doctoral Researcher, Department of Flow Physics and Technology, T.Michelis@tudelft.nl
‡Associate Professor, Department of Flow Physics and Technology, M.Kotsonis@tudelft.nl
§Ph.D. Researcher, Department of High-Speed Configurations, Juan.Franco@dlr.de
¶Research Scientist, Department of High-Speed Configurations, Stefan.Hein@dlr.de

II. Introduction

Modern aircraft wings are swept backwards to delay the occurrence of unwanted compressibility effects on the suction side of the wing. This wing configuration gives rise to an additional flow component within the boundary layer called the Crossflow (CF) component, see [1]. Laminar-to-turbulent transition in such three-dimensional boundary layers is commonly dominated by the exponential growth of stationary Crossflow Instabilities (CFI) in flows with low freestream turbulence. CFI are known to be extremely sensitive to both distributed and isolated roughness and surface protuberances on the wing surface. However, accounting for rapid geometrical features poses significant challenges to flow stability and transition prediction methodologies.

The stability of two-dimensional boundary layers (i.e. unswept) over smooth wall protuberances (i.e. humps) was studied in e.g. [2, 3]. Results clearly indicate the local and downstream significance of accounting for surface protuberances in a transition scenario dominated by Tollmien-Schlichting (TS) instabilities. It was shown by Hein [4] and Theofilis et al. [5] that the Parabolized Stability Equations (PSE) methodology is an effective tool to assess the instability in flows with thin separation bubbles. This holds for both linear and nonlinear instability analyses. Thus the rise of separation bubbles thus might not be a limiting factor to the application of the PSE methodology. Gao et al. [2] showed a validation of the linear PSE implementation over humps with reversed flow regions. However, a validation of the curvilinear implementation as well as a verification of the PSE assumption of slowly varying flow was lacking for the presented case. Franco et al. [3] instead shows that the Parabolized Stability Equations (PSE) are unable to correctly predict the stability in the vicinity of specific hump shapes. Instead, a method based on the Adaptive Harmonic Linearized Navier-Stokes (AHLNS) equations proved very accurate. This was reiterated by Tocci et al. in [6] concluding that the use of PSE should be avoided in flows featuring sharp geometries of wall protuberances, though it could be used in some flows over smooth irregularities. In 2013, Park and Park [7] showed an extension of the PSE method to nonlinear stability over a smooth hump and compared the results with Direct Numerical Simulations (DNS) from Wörner et al. [8]. Local differences between DNS and the PSE were shown. However, Park and Park attributed this deviation to a difference in hump shape with the results from Wörner et al. [8]. More recently, Park and Oh [9] investigated the effect of hump shape on the stability of two-dimensional boundary layers showing a destabilization of the incoming modes for all cases.

While a wealth of past studies has treated two-dimensional, TS-dominated flows, considerably less knowledge is available in the case of three-dimensional, CFI-dominated flows. Cooke et al. [10] analyzed the stability of a swept-wing boundary layer subject to forward- and backward-facing steps using Linear Stability Theory (LST), Parabolised Stability Equations and Linearized Harmonic Navier–Stokes (LHNS) despite this case clearly violating the parallel flow and slowly varying flow assumptions present in LST and PSE, respectively. They conclude that the PSE indeed "fails to correctly capture the effects of the steps" and that the LHNS is more physically correct. A systematic analysis of the limits of the PSE framework in cases with strong local curvature is currently not available. However, Tocci et al. [6] suggest to use the relative importance of streamwise and wall-normal gradients in the base flow to assess the validity of the slowly varying flow assumption in PSE. Additionally, they note that the application of PSE is dubious if the length scale of streamwise variations introduced by surface irregularities is of the same order as the instability's streamwise wavelength.

Despite the known significance of surface protuberances to the transition scenario, the body of literature on the stability of three-dimensional boundary layers over smooth protuberances is lacking. To the authors' best knowledge, no publication currently exists examining the interactions between incoming stationary crossflow instability disturbances and a two-dimensional hump. Recent studies have performed various Direct Numerical Simulations (DNS), stability analysis and experiments on steps, e.g. [10–12], that provide valuable insight in the flow mechanics, though the conclusions cannot be directly extended to the interaction with smooth geometries.

After an introduction to the setup (Section III) and methodology (Section IV), the effect of hump size is first investigated by linear stability analysis and the limit of the PSE assumption is then assessed for the primary mode. This analysis is then extended by comparing nonlinear stability predictions of PSE and HNS. In doing so, a first indication is given of the limits in wall deformation geometry for which the PSE assumptions are not valid. Nonlinear simulations are used to identify the effect of the considered wall geometries on the nonlinear evolution of the incoming crossflow instabilities. Lastly, the work will also consider the interaction of the incoming disturbance with the protuberance through energy exchange budgets. A conclusion is then presented on both the physics of the interaction, as well as the viability of the numerical frameworks used to predict this interaction.

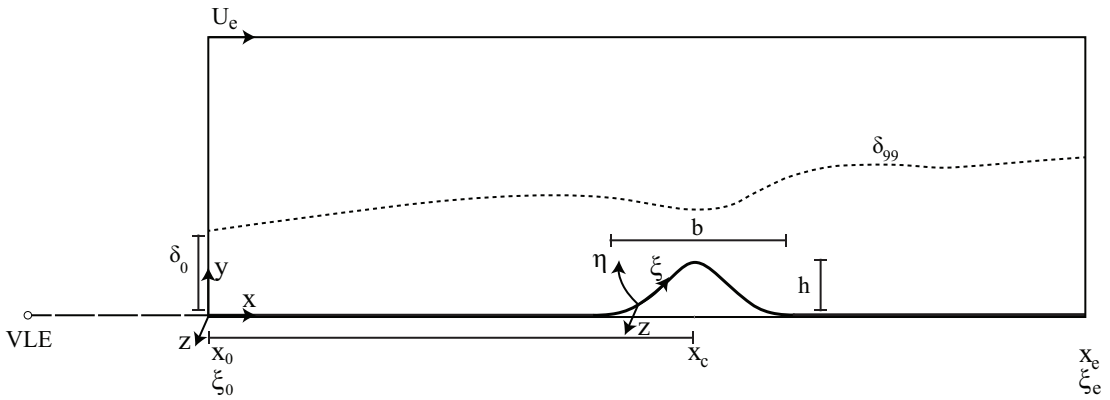

Fig. 1 Schematic of the problem showing the computational domain and coordinate systems, base flow, Virtual Leading Edge (VLE) and protuberance dimensions. (Note: the shown protuberance shape is only for illustration purposes, the exact shape is not shown)

III. Problem Statement

The stability of boundary layers over wall protuberances on a 45° swept plate subject to a favourable pressure gradient is considered. The base case is adjusted from the experiments of Rius-Vidales and Kotsonis [12]. The experiments feature a swept symmetrical wing named the M3J, see [13]. At a chord-based Reynolds number of $2.3 \cdot 10^6$ and a moderate angle of attack (3 degrees), the crossflow instability mode that is most amplified upstream of the transition point is characterized by a spanwise wavelength $\bar{\lambda}_z = 7.5$ mm [12] and its angular frequency $\omega = 0$. This mode is fully stationary. Sharp forward-facing steps were then mounted on the wing at a chord-wise location of $\frac{x}{c} = 20\%$. Some shallow steps were found to locally stabilize the primary stationary mode and its harmonics. However, the majority of studied geometries resulted in a notable transition advancement. The results of Rius Vidales expose the need for a systematic analysis of the interaction of wall protuberances and stationary CFI in a fast and efficient manner. This approach can guide and inform future experimental investigations and at the same time provide insights in the physical interpretation of the outcomes. The aim of the present work is to survey a range of different stability analysis methods, for a nominal test problem, namely smooth protuberances.

Here, the effect of smooth surface deformations of varying shapes and sizes are thus analyzed for the same flow topology. This wall deformation is centered at 20% of the chord. The flow conditions from the experiments of Rius-Vidales and Kotsonis [12] are matched by imposing the experimentally measure external pressure at the top boundary for base flow computations (see section IV). The inflow of the computational domain is set at a chord-based location of 5% as shown in figure 1. The Cartesian coordinate system $[x, y, z]$ is swept with the wing such that the x axis is orthogonal to the leading edge. The body-fitted coordinate system $[\xi, \eta, z]$ used for stability calculations is similarly swept.

The smooth protuberances are placed at $\frac{x}{c} = 0.2$, or $x = 238.3$, and are characterized by their height, h, and width, b. A total of 10 cases are considered, including the clean case A for which no protuberance is present. The height, widths and names of all protuberances are shown in table 1. The exact wall shape is not shown.

The protuberances of cases B1, C2 and D3 have a constant aspect ratio ($b = 16h$), but vary in overall size. The boundary layer stability for these cases is analyzed to observe the effect of protuberance size on incoming stationary crossflow instabilities. A variation in height for equal width, as is present in cases B1-B4, C2-C4 and D3-D4, will be used to provide insight in the limitations of the PSE methodology for the currently analyzed protuberances. In addition to the cases presented in table 1, a clean case A, void of any surface protuberance, is analyzed for validation and comparison purposes.

Table 1 Considered cases described by protuberance height and width

		b			
		0	9.4	12	14.5
h	0	A			
	0.59		B1		
	0.75		B2	C2	
	0.97		B3	C3	D3
	1		B4	C4	D4

IV. Methodology

A basic flow state that describes the steady, unperturbed solution to the Navier-Stokes equations is required as input to the considered stability analysis methods. For this, the finite element Navier-Stokes solver in COMSOL is used (see [14]). A numerical domain with height $H = 51.9$ and length $L = 454$ is discretized in second order basis functions, with 115 elements in the wall-normal direction that are clustered near the wall. In the streamwise direction, 945 elements are present with a local refinement around the surface protuberance. In the spanwise z-direction, two elements are present and periodic boundary conditions are imposed. Both pressure and velocities are solved using second-order finite elements. Due to the upstream truncation of the domain at x_0, there exists a virtual leading edge upstream of the computational domain. Therefore, a pre-calculated three-dimensional boundary layer profile is prescribed at the inflow. The local solution of the Falkner-Skan-Cooke equations is used to this extent. The bottom wall imposes the no-slip condition. An experimentally determined favourable pressure gradient from [12] is adjusted as shown by [11] and imposed on the top boundary condition. At the outflow, a constant static pressure is prescribed that matches the local top boundary pressure. The streamwise base flow velocity contours around the surface protuberances for all cases are shown in figure7. Some flow separation can be seen in cases B3, C4 and D4. The maximum reverse flow velocity is less than 2% of the local external velocity.

The PSE, HNS and AHLNS methodologies are used to evaluate the stability of stationary crossflow modes over various wall deformations. The fundamentally different nature of PSE (parabolized, nonlinear), AHLNS (elliptic, linear) and HNS (elliptic, nonlinear) is used to draw conclusions regarding the interaction between the incoming perturbation and the wall deformation. The PSE neglect second-order streamwise derivatives of the perturbation shape function, but account for wave-triad interactions. The AHLNS methodology instead neglects nonlinear terms while maintaining higher order streamwise gradients in the perturbation equations. Finally, the HNS are used to solve the nonlinear perturbation equations without further assumptions. All three aforementioned methods are based on the incompressible NS equations:

$$\frac{\partial u}{\partial t} + u\frac{\partial u}{\partial x} + v\frac{\partial u}{\partial y} + w\frac{\partial u}{\partial z} = \frac{\partial p}{\partial x} + \frac{1}{Re}\left(\frac{\partial^2 u}{\partial x^2} + \frac{\partial^2 u}{\partial y^2} + \frac{\partial^2 u}{\partial z^2}\right), \tag{1a}$$

$$\frac{\partial v}{\partial t} + u\frac{\partial v}{\partial x} + v\frac{\partial v}{\partial y} + w\frac{\partial v}{\partial z} = \frac{\partial p}{\partial y} + \frac{1}{Re}\left(\frac{\partial^2 v}{\partial x^2} + \frac{\partial^2 v}{\partial y^2} + \frac{\partial^2 v}{\partial z^2}\right), \tag{1b}$$

$$\frac{\partial w}{\partial t} + u\frac{\partial w}{\partial x} + v\frac{\partial w}{\partial y} + w\frac{\partial w}{\partial z} = \frac{\partial p}{\partial z} + \frac{1}{Re}\left(\frac{\partial^2 w}{\partial x^2} + \frac{\partial^2 w}{\partial y^2} + \frac{\partial^2 w}{\partial z^2}\right), \tag{1c}$$

$$\frac{\partial u}{\partial x} + \frac{\partial v}{\partial y} + \frac{\partial w}{\partial z} = 0, \tag{1d}$$

where p is the static pressure and u, v and w are the total velocities in respectively the streamwise direction x, the wall-normal direction y and the spanwise direction z. The equations are nondimensionalized by the reference velocity $\bar{U}_e = 15.1$ m/s, the boundary layer thickness at the inflow $\bar{\delta}_0 = 7.71 \cdot 10^{-4}$ m shown in figure 1 and the kinematic viscosity $\bar{\nu} = 1.4711 \cdot 10^{-5}$ m^2/s, resulting in a global reference Reynolds number $Re = \frac{\bar{U}_0 \bar{\delta}_0}{\bar{\nu}} = 791.4$. The bars denote dimensional quantities.

The velocities and pressure are decomposed as the sum of the steady base flow, $\mathbf{Q} = [U\ V\ W\ P]^T$, and unsteady perturbations, $\mathbf{q}' = [u'\ v'\ w'\ p']^T$. The base flow terms are subtracted from the equations to arrive at the perturbation equations. In addition, a coordinate transformation is performed to the body-fitted $\xi\eta$-coordinates. The ξ axis, for which $\eta = 0$, follows the wall. The grid is then generated elliptically ensuring orthogonality at the wall. The transformation results in the generalized perturbation equations:

$$
\begin{aligned}
&\frac{\partial u'}{\partial t} + U\frac{\partial u'}{\partial \xi}\xi_x + U\frac{\partial u'}{\partial \eta}\eta_x + u'\frac{\partial U}{\partial x} + u'\frac{\partial u'}{\partial \xi}\xi_x + u'\frac{\partial u'}{\partial \eta}\eta_x + V\frac{\partial u'}{\partial \xi}\xi_y \\
&+ V\frac{\partial u'}{\partial \eta}\eta_y + v'\frac{\partial u}{\partial \xi}\xi_y + v'\frac{\partial u}{\partial \eta}\eta_y + v'\frac{\partial U}{\partial y}\xi_y + W\frac{\partial u'}{\partial z} + w'\frac{\partial U}{\partial z} + w'\frac{\partial u'}{\partial z} = \\
&- \frac{\partial p'}{\partial \xi}\xi_x - \frac{\partial p'}{\partial \eta}\eta_x + \frac{1}{Re}\left(\frac{\partial^2 u'}{\partial \xi^2}\xi_x^2 + \frac{\partial^2 u'}{\partial \eta^2}\eta_x^2 + 2\xi_x\eta_x\frac{\partial^2 u'}{\partial \xi\partial \eta} + \frac{\partial u'}{\partial \xi}\xi_{xx}\right. \\
&\left. + \frac{\partial u'}{\partial \eta}\eta_{xx} + \frac{\partial^2 u'}{\partial \xi^2}\xi_y^2 + \frac{\partial^2 u'}{\partial \eta^2}\eta_y^2 + 2\xi_y\eta_y\frac{\partial^2 u'}{\partial \xi\partial \eta} + \frac{\partial u'}{\partial \xi}\xi_{yy} + \frac{\partial u'}{\partial \eta}\eta_{yy} + \frac{\partial^2 u'}{\partial z^2}\right),
\end{aligned} \tag{2a}
$$

$$
\begin{aligned}
&\frac{\partial v'}{\partial t} + U\frac{\partial v'}{\partial \xi}\xi_x + U\frac{\partial v'}{\partial \eta}\eta_x + u'\frac{\partial V}{\partial x} + u'\frac{\partial v'}{\partial \xi}\xi_x + u'\frac{\partial v'}{\partial \eta}\eta_x + V\frac{\partial v'}{\partial \xi}\xi_y \\
&+ V\frac{\partial v'}{\partial \eta}\eta_y + v'\frac{\partial v}{\partial \xi}\xi_y + v'\frac{\partial v}{\partial \eta}\eta_y + v'\frac{\partial V}{\partial y} + W\frac{\partial v'}{\partial z} + w'\frac{\partial V}{\partial z} + w'\frac{\partial v'}{\partial z} = \\
&- \frac{\partial p'}{\partial \xi}\xi_y - \frac{\partial p'}{\partial \eta}\eta_y + \frac{1}{Re}\left(\frac{\partial^2 v'}{\partial \xi^2}\xi_x^2 + \frac{\partial^2 v'}{\partial \eta^2}\eta_x^2 + 2\xi_x\eta_x\frac{\partial^2 v'}{\partial \xi\partial \eta} + \frac{\partial v'}{\partial \xi}\xi_{xx}\right. \\
&\left. + \frac{\partial v'}{\partial \eta}\eta_{xx} + \frac{\partial^2 v'}{\partial \xi^2}\xi_y^2 + \frac{\partial^2 v'}{\partial \eta^2}\eta_y^2 + 2\xi_y\eta_y\frac{\partial^2 v'}{\partial \xi\partial \eta} + \frac{\partial v'}{\partial \xi}\xi_{yy} + \frac{\partial v'}{\partial \eta}\eta_{yy} + \frac{\partial^2 v'}{\partial z^2}\right),
\end{aligned} \tag{2b}
$$

$$
\begin{aligned}
&\frac{\partial w'}{\partial t} + U\frac{\partial w'}{\partial \xi}\xi_x + U\frac{\partial w'}{\partial \eta}\eta_x + u'\frac{\partial W}{\partial x} + u'\frac{\partial w'}{\partial \xi}\xi_x + u'\frac{\partial w'}{\partial \eta}\eta_x + V\frac{\partial w'}{\partial \xi}\xi_y \\
&+ V\frac{\partial w'}{\partial \eta}\eta_y + v'\frac{\partial w}{\partial \xi}\xi_y + v'\frac{\partial w}{\partial \eta}\eta_y + v'\frac{\partial W}{\partial y} + W\frac{\partial w'}{\partial z} + w'\frac{\partial W}{\partial z} + w'\frac{\partial w'}{\partial z} = \\
&- \frac{\partial p'}{\partial z} + \frac{1}{Re}\left(\frac{\partial^2 w'}{\partial \xi^2}\xi_x^2 + \frac{\partial^2 w'}{\partial \eta^2}\eta_x^2 + 2\xi_x\eta_x\frac{\partial^2 w'}{\partial \xi\partial \eta} + \frac{\partial w'}{\partial \xi}\xi_{xx}\right. \\
&\left. + \frac{\partial w'}{\partial \eta}\eta_{xx} + \frac{\partial^2 w'}{\partial \xi^2}\xi_y^2 + \frac{\partial^2 w'}{\partial \eta^2}\eta_y^2 + 2\xi_y\eta_y\frac{\partial^2 w'}{\partial \xi\partial \eta} + \frac{\partial w'}{\partial \xi}\xi_{yy} + \frac{\partial w'}{\partial \eta}\eta_{yy} + \frac{\partial^2 w'}{\partial z^2}\right),
\end{aligned} \tag{2c}
$$

$$
\frac{\partial u'}{\partial \xi}\xi_x + \frac{\partial u'}{\partial \eta}\eta_x + \frac{\partial v'}{\partial \xi}\xi_y + \frac{\partial v'}{\partial \eta}\eta_y + \frac{\partial w'}{\partial z} = 0. \tag{2d}
$$

The PSE, AHLNS and HNS approaches are described here in short in addition to the respective discretization of the equations. The initial condition for all methods is generated through solving the local eigenvalue stability problem for the shape function and wave number, although the resulting wave number is not used in HNS. All methods were subjected to a grid convergence study.

A. Parabolized Stability Equations

The nonlinear PSE are derived from the perturbation equations by assuming a nonlinear perturbation ansatz as:

$$
\mathbf{q}'(\xi,\eta,z,t) = \sum_{m=-M}^{M}\sum_{n=-N}^{N} \hat{\mathbf{q}}_{m,n}(\xi,\eta) e^{i\left(\int_{\xi_0}^{\xi_e} \alpha_{m,n} d\xi^* + \beta_n z - \omega_m t\right)}, \quad \beta,\omega \in \mathcal{R}; \quad \hat{q},\alpha \in C, \tag{3}
$$

where α is the complex-valued streamwise wavenumber, β the real-valued spanwise wavenumber and ω is the angular frequency. The subscripts of β and ω, n and m respectively, indicate the wave specifications of mode (m,n) with respect to the mode (1,1) as $\beta_n = n\beta_1$ and $\omega_m = m\omega_1$ truncated at $n = N$ and $m = M$. However, here $\omega_m = 0$ for all

m and $\beta_1 = 0.6459$ (corresponding to the 7.5 mm mode in Rius Vidales experiments) since only stationary crossflow instabilities are considered. The modal sum is truncated at $N = 5$, as the addition of higher modes was found not to affect the results. The imaginary unit is denoted i. The computational domain ranges from ξ_0 to ξ_e. The * annotation, in $d\xi^*$, indicates the integration variable. A more detailed derivation in Cartesian coordinates can be found in [15, 16]. Here, however, the derivation is performed in generalized coordinates to be able to account for the (local) curvature of the protuberance. The parabolization assumption is made in the ξ direction and the grid for this case is generated ensuring orthogonality at the wall. The LPSE and NPSE equations can be written in matrix form as:

$$[L]\hat{\mathbf{q}}_{m,n} + [M]\frac{\partial \hat{\mathbf{q}}_{m,n}}{\partial \xi} + [N]\frac{\partial \alpha_{m,n}}{\partial \xi}\hat{\mathbf{q}}_{m,n} = \mathbf{r}_{m,n}, \tag{4}$$

where the right-hand side forcing, $\mathbf{r}$, comprises the nonlinear terms that are neglected in LPSE.

The equations are then discretized. Streamwise derivatives are approximated via a first-order backward Euler scheme. The streamwise direction is discretized with 200 equidistant stations. In the wall-normal direction, spectral differentiation is employed using a Chebyshev polynomial basis with 70 collocation points clustered near the wall, see [17, 18] for further details.

B. Adaptive Harmonic Linearized Navier-Stokes Equations

The AHLNS equations are derived from the perturbation equations by assuming a linear version of the PSE perturbation ansatz:

$$\mathbf{q}'(\xi,\eta,z,t) = \hat{\mathbf{q}}(\xi,\eta)e^{i\left(\int_{\xi_0}^{\xi_e} \alpha d\xi^* + \beta z - \omega t\right)}, \quad \beta,\omega \in \mathcal{R}; \quad \hat{q},\alpha \in C. \tag{5}$$

The main advantage of the adaptive approach is that it exploits the wave-like character of the convective instabilities in a similar fashion as in the PSE method. Thus, the spatial resolution of the numerical grid required in streamwise direction is significantly reduced when compared with HNS for linear computations. However, unlike to the PSE approach, two aspects are crucial in this approach: First, the streamwise wavenumber α is allowed to rapidly vary in the streamwise direction. Second, the adaptive approach does not introduce any further simplification in the system of equations, i.e. 2^{nd}-order derivatives in streamwise direction are maintained. A more detailed description of the AHLNS approach can be found in the works of Franco and Hein [19] and Franco et al. [3].

Since the perturbation ansatz of eq. 5 is similar to that of LPSE, the coupling between both methodologies (LPSE & AHLNS) is relatively straightforward. Therefore, the whole domain in streamwise direction is divided in three regions: 1) from the inflow up to $x = 142$, 2) from $x = 142$ up to $x = 390$, and finally, from $x = 390$ up to the outflow. This division is based on the local influence of the presence of a wall deformation on the base flow quantities, limited to region 2. Consequently, LPSE (here, NOLOT-PSE [20]) are used in regions 1 & 3, while AHLNS is applied in region 2 only. In principle, one could use AHLNS for the whole domain (1+2+3) without introducing any division, but then the efficiency of the marching procedure of the LPSE in regions 1 & 3 would be lost. For region 2, 150 points in both streamwise and wall-normal directions are used. A 4th-order centered scheme is employed to solve the AHLNS equations.

C. Harmonic Navier-Stokes Equations

A framework that employs the full nonlinear harmonic Navier-Stokes equations has been developed [21] which follows from the perturbation equations by assuming a nonlinear perturbation ansatz as:

$$\mathbf{q}'(\xi,\eta,z,t) = \sum_{m=-M}^{M}\sum_{n=-N}^{N} \hat{\mathbf{q}}_{m,n}(\xi,\eta)e^{i(\beta_n z - \omega_m t)}, \quad \beta,\omega \in \mathcal{R}; \quad \hat{q},\alpha \in C, \tag{6}$$

where all oscillations and growth are maintained in the shape functions. This approach is described by Appel in [22]. Consequently, as in AHLNS, higher order derivatives of $\hat{q}$ are not neglected. The nonlinear terms are also maintained and return in the final equations as an explicit forcing term on the right-hand side. The final equations can be written in the form:

$$[A]\hat{\mathbf{q}}_{m,n} + [B]\omega\hat{\mathbf{q}}_{m,n} + [C]\beta\hat{\mathbf{q}}_{m,n} + [D]\beta^2\hat{\mathbf{q}}_{m,n} + [E]\frac{\partial \hat{\mathbf{q}}_{m,n}}{\partial \xi} + [F]\frac{\partial^2 \hat{\mathbf{q}}_{m,n}}{\partial \xi^2} = \mathbf{r}_{m,n}. \tag{7}$$

As with the NPSE, the nonlinear terms enter the equations as the forcing term $\mathbf{r}$, which is iteratively converged in the solution procedure. The contents of the matrices of equation 7 can be found in the appendix.

Table 2 Discretization per method

Method	Streamwise differentiation	nx	wall-normal differentiation	ny
PSE	first-order backward	200	Pseudo-spectral	70
AHLNS (region 2)	4th-order central	150	4th-order central	150
HNS	4th-order central	1500	Pseudo-spectral	70

In the HNS solver, both the first-order and second-order streamwise derivatives are approximated via a 4th-order centered finite-difference scheme. The streamwise axis is discretized with 1500 locations according to a Gaussian distribution with refinement around the surface deformation. Wall-normal differentiation is performed the same way as in PSE via spectral differentiation using a Chebyshev polynomial basis on 70 wall-clustered collocation points.

Table 2 summarizes the information on discretization per method. However, A note is necessary here regarding the discretization and grid size details for each method. Due to their fundamentally different governing assumptions as well as different numerical implementations, each method is applied on a different numerical grid. Nevertheless, for the results in this study, all three methods have been subject to a grid refinement process and have converged, within truncation error. As such, any pertinent differences appearing in the results can be largely attributed to modeling assumptions, rather than grid resolution differences.

D. Boundary Conditions

Due to the common problem and geometry, all three stability analysis methods make use of commonalities in boundary conditions. However, depending on method some necessary changes are also implemented. At the inflow, the local linear stability problem is solved and an amplitude is imposed on the resulting eigenfunction to provide the inflow condition. At the curved wall ($\eta = 0$), the no-slip condition is imposed by forcing the perturbation velocities to be 0. Similarly, the perturbations should exponentially decay into the freestream and perturbation velocities are therefore set to 0 at the top boundary. Perturbation pressure is solved for implicitly in all three methods, thus not requiring boundary conditions. Due to the parabolic approximation and adaptive technique respectively, the PSE and AHLNS implementations do not require a specific outflow condition. In HNS however, an outflow buffer is required to damp the amplitude of the perturbations and prevent upstream reflections. This outflow buffer is applied directly on the perturbations and ensures that the amplitudes are smoothly following a hyperbolic tangent [23–25].

V. Results

The HNS, NPSE and AHLNS were used to predict the (nonlinear) stability of swept wing boundary layers with smooth wall deformations. The effect of protuberance size, nonlinearities, the slowly varying flow assumption of PSE and the interaction of incoming perturbations with the wall deformation are considered separately.

A. Effect of Protuberance Size and Shape on Instability Development

The effect of the size of the wall deformation can be investigated by comparing the linear stability results of cases B1, C2, and D3. The width-to-height ratio of 16 is maintained as the overall is increased. Additionally, these simulations help verify the coordinate transformation performed for the generalized PSE and HNS codes.

Figure 2 shows the evolution of the amplitude and the imaginary component of streamwise wavenumber (i.e. growth rate) of the incoming crossflow perturbation. The amplitude is defined here as the maximum of the absolute streamwise perturbation velocity, $|u'|_{max}$. The amplitude evolution is only marginally affected by the deformation of the wall. The imaginary component of the streamwise wavenumber, shown in figure 2 (c), describes the growth rate which is the primary focus of this comparison as the cumulative effect on the downstream evolution is marginal. In HNS, this growth rate is not present and is calculated a-posteriori based on the maximum streamwise perturbation velocity following:

$$\alpha = \frac{1}{i\, u'_{max}} \frac{\partial u'}{\partial \xi}\Big|_{y=y_{u_{max}}}, \tag{8}$$

where $y_{u_{max}}$ corresponds to the location where the absolute streamwise perturbation is maximum. The imaginary component of α is the growth rate.

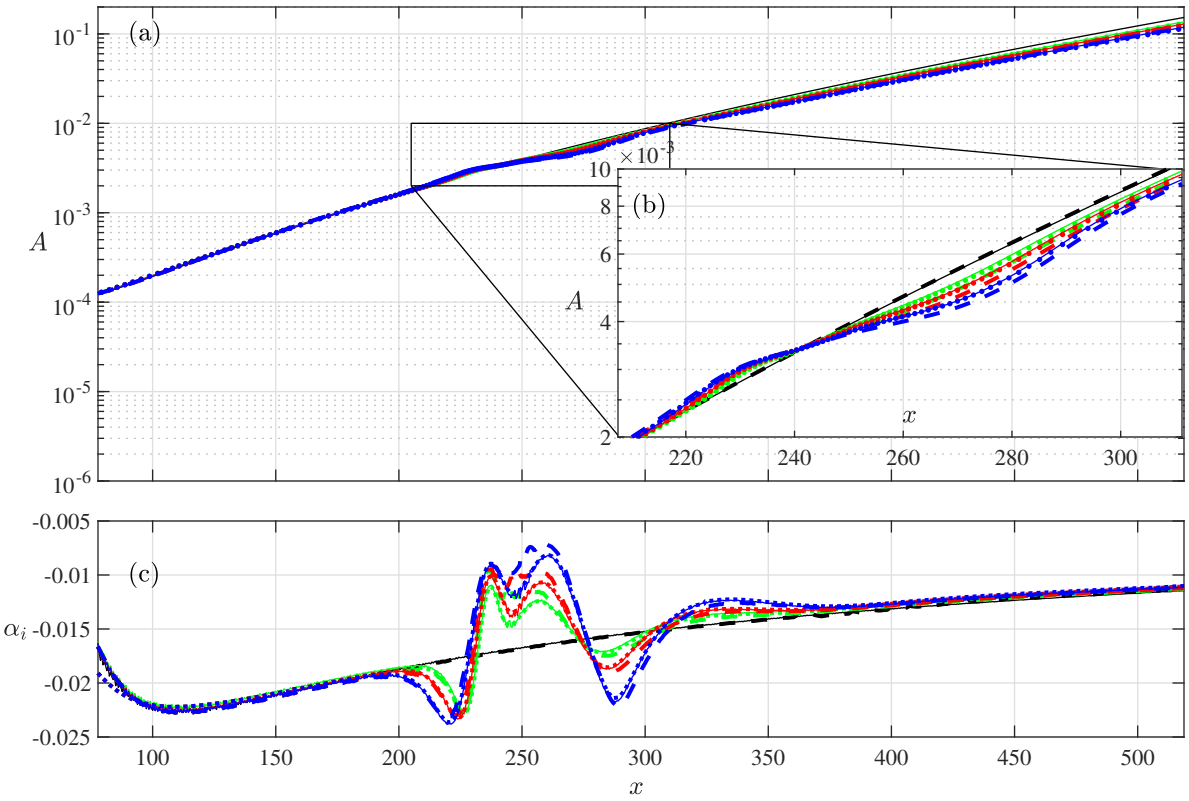

Fig. 2 Amplitude evolution (a), close-up view (b) and growth rates (c) for the clean case (black), case B1 (green), case C2 (red) and case D3 (blue) as calculated by LPSE (dashed line), HNS (solid line) and AHLNS (dots)

The growth rates predicted by PSE, AHLNS and HNS match closely, though the PSE slightly overpredicts the response to the wall curvature. The stability response is magnified when the size is increased. For all cases presented in figure 2, a minor stabilization of the primary mode can be seen with respect to the clean flat plate case.

Figure 3 (a) shows the amplitude development for cases B4, C4, and D4 as calculated by linear PSE, HNS and AHLNS. The varying width of these cases results in strongly varying gradients in the base flow. The stability response is therefore less comparable between the cases compared to figure 2. The PSE predicts a linear amplitude development closely matching with HNS and AHLNS for all cases. The discontinuity of the growth rate, α_i, in figure 3 (b) is an artefact of the change in monitoring location of the maximum amplitude.

B. Nonlinear Effects and Behaviour of Higher Harmonics

Figures 4 (a) and (b) show the linear and nonlinear ($N = 5$) amplitude development for the primary crossflow instability and accompanying harmonics of cases B1 and D3. Nonlinearities start being visible in the growth of the primary mode around the location of the wall deformation as indicated by the prediction of linear HNS. In these nonlinear scenarios, the primary mode is still stabilized due to the presence of the protuberance for both cases. The primary mode shape or and amplitude are not strongly altered by the presence of the wall deformations shown here. The higher harmonics experience similar growth trend where the growth is first damped. This is a direct consequence of the primary mode being damped, resulting in a decrease in the strength of the nonlinear interactions on all harmonics. Slightly more downstream, around $x = 250$, a strong amplification follows for all higher harmonics $n > 1$. The mean flow distortion sees a similar response to the higher harmonics slightly further upstream. Despite this strong rise in amplitudes, no direct effect is seen in the primary mode other than the strength of nonlinearities being locally increased.

The response of the primary mode and that of the higher harmonics is analyzed later in section V.D using a Reynolds-Orr energy budget analysis.

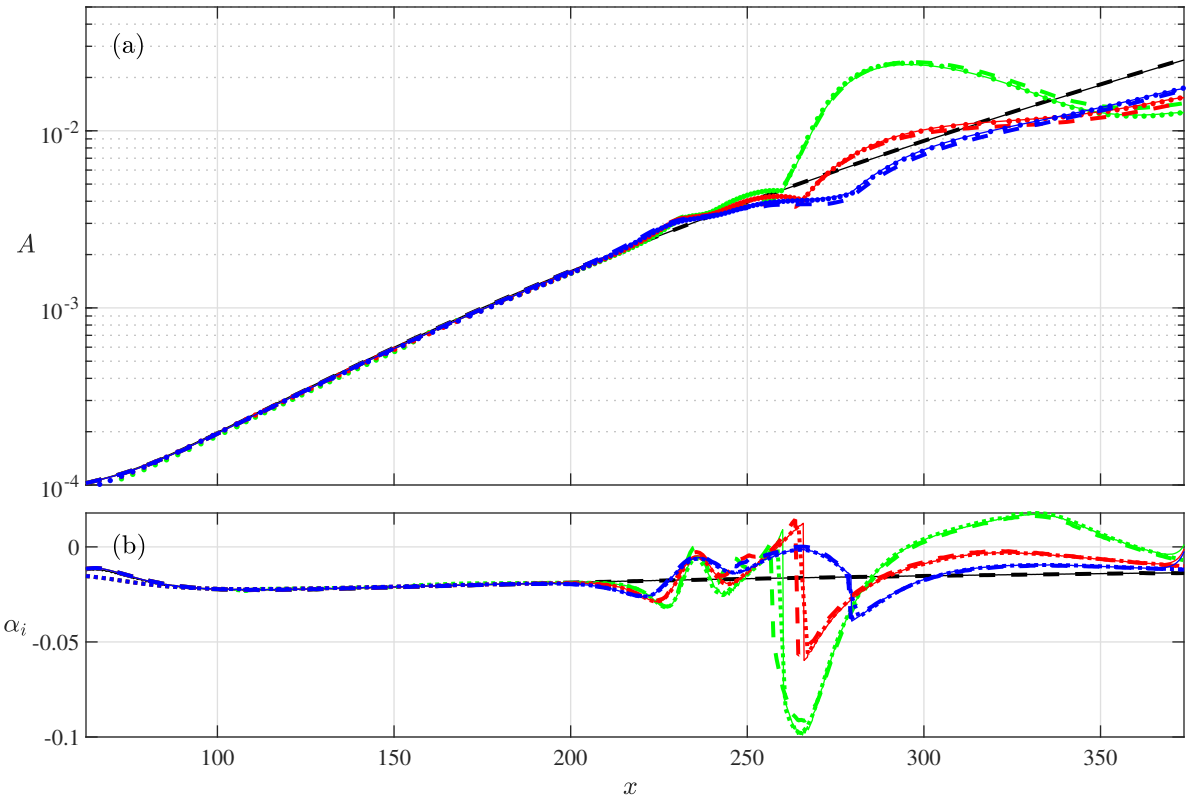

Fig. 3 Amplitude evolution (a) and growth rates (b) for the clean case (black), case B4 (green), case C4 (red) and case D4 (blue) as calculated by LPSE (dashed line), HLNS (solid line) and AHLNS (dots)

C. Limitations of the PSE Methodology

The PSE framework assumes slowly varying perturbation shape in the streamwise direction. The limit of this assumption is sought for various wall deformation shapes. Linear simulations showed that the PSE framework performs well for cases with smooth wall deformations. In nonlinear simulations however, the NPSE was not able to converge to a solution for all cases. This indicates an upper limit to the framework's validity governed by higher harmonics, the mean flow distortion or its interactions. The stability results that are available are compared in terms of amplitude and shape function to evaluate how accurate the PSE framework is. It is noted that nonlinearities complicate the analysis of the results as growth rates are no longer an amplitude-independent metric. Therefore, amplitudes are used instead to observe any deviations from the HNS result.

Figures 4 (a) and (b) show the nonlinear stability development as calculated by NPSE (red) and HNS (black) for cases B1 and D3, respectively. Previously, in figure 2, it was shown that the PSE was able to predict the linear stability accurately for these cases. A close match was also found for the nonlinear stability. A quantitative difference can be seen in the response of higher harmonics around the protuberance as the PSE predicts a smaller and slower rise of amplitudes. Nevertheless, the effect on the primary mode is negligible. For higher amplitudes this might prove significant.

The ability of PSE to find the correct nonlinear stability response for the cases presented in this work is shown via a maximum difference in N-factor, ΔN, over the domain compared to HNS for the primary mode in table 3. This metric was chosen since the perturbations nonlinearly saturate shortly downstream of the center of the deformation which could reduce the perceived error of the PSE assumption if the N-factor at the outflow is taken. The HNS framework was able to converge the nonlinear problem for all cases except B4 which showed a strong destabilizing response of the second harmonic. The PSE framework failed to converge for cases B3, B4 and C4. The limit of the PSE assumption therefore lies between cases B2 and B3 and cases C3 and C4. However, it should be noted that the error between PSE and HNS was significant already for cases C2, C3 and D4 with $\Delta N \approx 0.39 - 0.58$ despite the PSE's ability to converge to a solution. The linear development of the primary mode computed by AHLNS, and HNS shows an excellent agreement

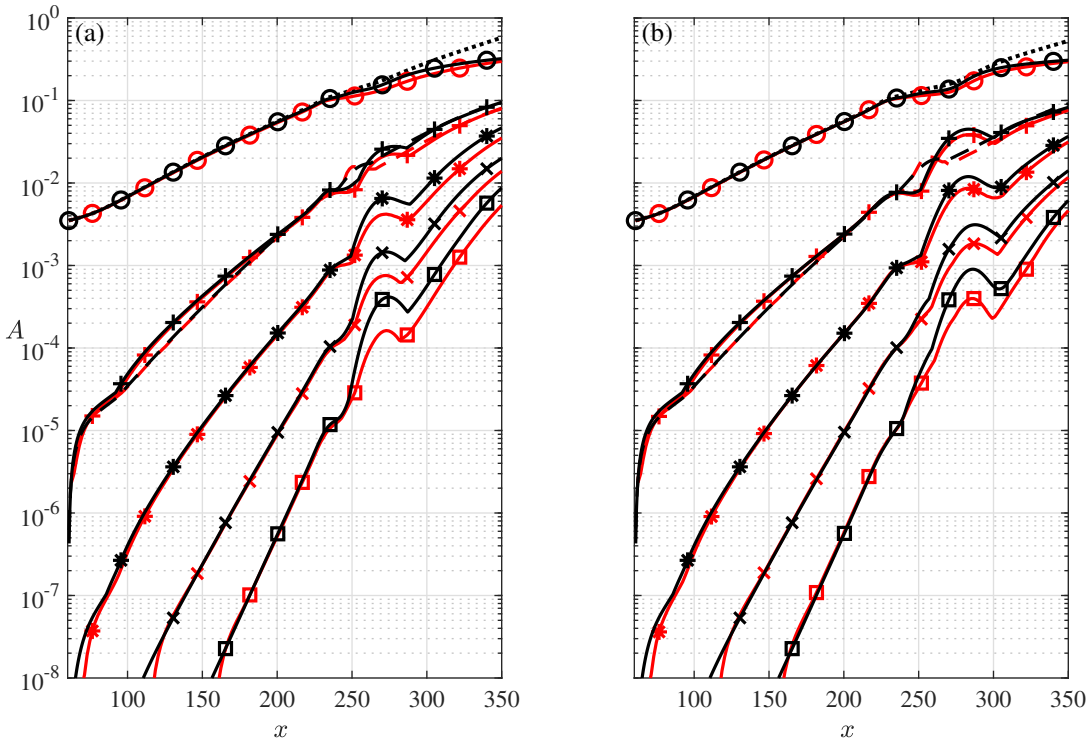

Fig. 4 Case B1 (a) and case D3 (b) Linear (dotted) and nonlinear (solid lines) amplitude ($|u'|_{max}$) development of the crossflow instability characterized by $\beta = 0.65$ (o) in addition to the development of the mean flow distortion (dashed), second harmonic (+), third harmonic ($*$), fourth harmonic (x) and fifth harmonic ($\square$) as predicted by HNS (black) and NPSE (red)

for all cases considered in the present study.

Table 3 Maximum N-factor difference ΔN between HNS and PSE based on the primary mode development per case

	B	C	D
1	0.105		
2	0.388	0.111	
3	-	0.495	0.107
4	-	-	0.583

A comparison between perturbation shape functions can be found in figure 5 for the streamwise component of the primary mode. Figure 6 shows a comparison of the wall-normal perturbation velocity of the mean flow distortion for case B1. Not all components, harmonics and locations can be shown. A close match is found for all but the mean flow distortion's wall-normal velocity after the apex. The deviation from HNS is significant even for the small shallow hump that is present for this case. As the protuberance reconnects to the flat wall, the PSE solution converges again to the HNS solution in terms of normalized perturbation shape while some amplitude discrepancies remain. The mismatch is considered a direct result of neglecting the higher order derivatives of the perturbation shape function. For the wall-normal velocity component especially, higher-order streamwise derivatives proved significant.

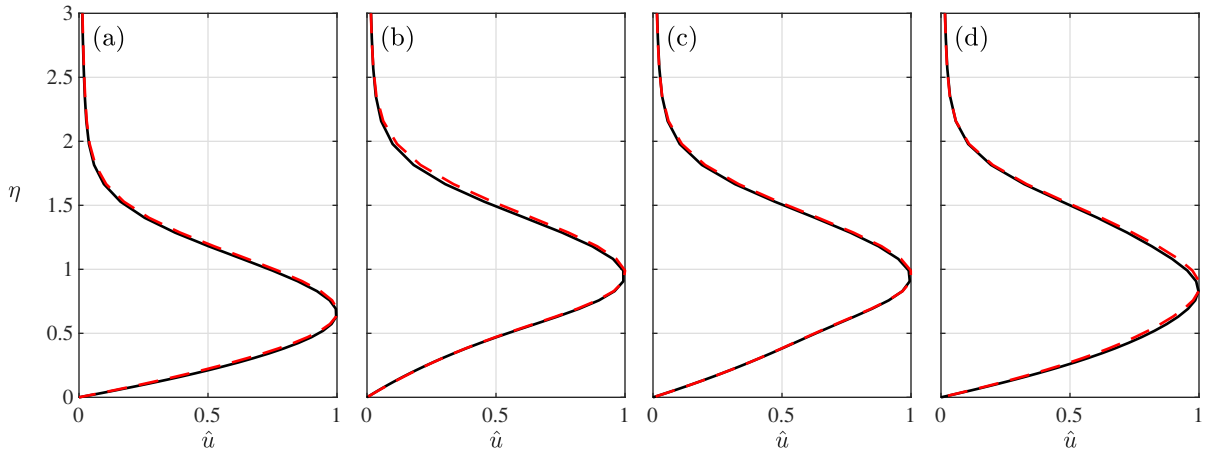

Fig. 5 Normalized streamwise perturbation shape function of the primary mode as per HNS (black, solid) and NPSE (red, dashed) at (a) $x = 238$, (b) $x = 250$, (c) $x = 259$, and (d) $x = 272$ for case B1

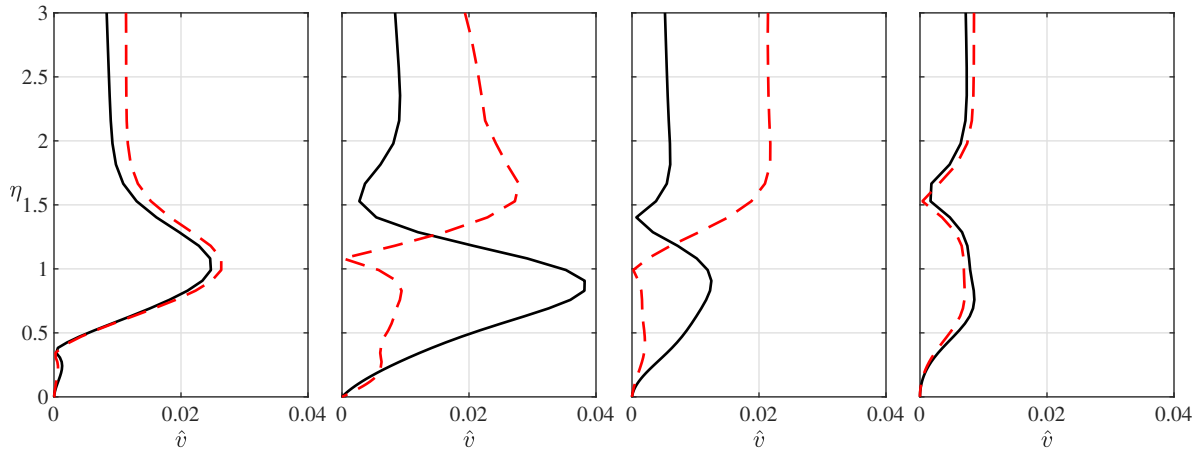

Fig. 6 Normalized wall-normal perturbation shape function of the mean flow distortion as per HNS (black, solid) and NPSE (red, dashed) at (a) $x = 238$, (b) $x = 250$, (c) $x = 259$, and (d) $x = 272$ for case B1

D. Mechanism of the Interaction between Wall Deformation and CFI

To gain more insight into the mechanism of the interaction of incoming stationary crossflow instability with the surface protuberances, the total flow field is analysed through a Fourier decoupled energy budget analysis of the Reynolds-Orr equations. For this analysis, the methodologies presented in Lanzerstorfer and Kuhlmann [26] as well as Casacuberta et al. [27] are utilised. The derivation leads to a Fourier-decoupled scalar kinetic energy budget equation that is well suited to correlate various sets of terms in the stability equations to the development of the perturbation flow field. For conciseness, the analysis is presented here only for the case D3. Additionally, only the energy budget of the nonlinearly developed primary mode and second harmonic are considered here. Although the same analysis can be applied to the higher harmonics and the mean flow distortion, [27] states the behaviour of higher harmonics is comparable to that of the second harmonic and no further insight can be gained from such an analysis. This statement is also supported by the amplitude development seen in figure 4

The Reynolds-Orr energy budget contours in the vicinity of the wall deformation can be seen in figures 8 (a-e) for the primary mode and 8 (f-j) for the second harmonic. The primary mode experiences a relative stabilization just downstream the apex ($x = 238.3$) which appears to be driven by linear production terms near the wall. This is also supported by the fact that this stabilization was captured in linear simulations (see figure 2). Nonlinear effects on the primary mode can be seen to be net negative despite a positive contribution to the energy budget that can be seen around

$\eta = 1$. For the second harmonic, the nonlinear interactions result in a net negative effect around $x = 240$ as the primary mode stabilizes, while become strongly positive downstream as the linear effect fades and amplitudes are reduced from elevated levels. The work done by viscous and pressure forces is of a smaller order and does not appear to be the driver of the discovered behaviour of any of the instabilities.

VI. Conclusion

Linear and nonlinear simulations were performed for swept wing boundary layers featuring varying surface deformations using the Parabolized Stability Equations, Adaptive Harmonic Linearized Navier-Stokes and Harmonic Navier-Stokes equations. The goal of this study was to gain more insight into the interaction between stationary crossflow instabilities and smooth surface protuberances and the ability of the PSE framework to find the spatial development of stationary crossflow instabilities in such flows.

The effect of the protuberance size was investigated alongside the mechanism of its interaction with incoming stationary crossflow instabilities. For the cases presented here, it was shown that the response to an equal surface geometry of greater size resulted in a stronger response following a similar pattern. This process starts slightly upstream of the protuberance where primary mode is destabilized. This is followed by alternating stabilization and destabilization until the growth rate converges to that of the flat plate. For the cases presented here, all protuberances resulted in a net stabilization of the incoming mode compared to the flat plate. The behaviour of the instability appears to be governed by linear mechanisms for the investigated amplitude and cases.

Comparing nonlinear simulations with a purely linear result, the effect of nonlinearities was seen to become significant around the location of the protuberance. Nevertheless, the main effect on the growth rate of the primary mode was driven by linear mechanisms. It was found that all higher harmonics experience a qualitatively similar rapid growth shortly downstream of the protuberance center. This rise appears to be governed by linear processes as production terms were seen to be responsible for a strong energy influx. It is succeeded by a decline in amplitude as these linear mechanisms fade and nonlinear interactions are not able to drive further growth.

Both linear and nonlinear PSE simulations were performed or attempted for all cases presented in this work. In linear simulations, the PSE framework proved fast and was able to closely match the results from linear HNS and AHLNS computations. AHLNS and PSE computations could be performed linearly requiring only a fraction of the streamwise resolution used for linear HNS computations due to the streamwise wavenumber present in the ansatz. When nonlinearities are accounted for, some disparity can be found in amplitude and mean flow distortion shape function calculted by NPSE compared to HNS. This holds for even the smallest surface protuberance geometry presented here. This difference is limited to amplitude for the primary mode as shape functions match closely. The mean flow distortion shows a significant deviation for the wall-normal velocity compared to HNS computations. Nevertheless, PSE proved capable of accounting for small humps in stability calculations qualitatively. Without validation through elliptic methods however, the results can only be used as an indication of the stability response. It is recommended to perform stability calculations around similar flow problems with a harmonic Navier-Stokes approach.

Acknowledgments

Authors S. Westerbeek, T. Michelis and M. Kotsonis were supported by the European Research Council (ERC) under the GLOWING project, grant number 803082.

References

[1] Haynes, T. S., and Reed, H. L., "Simulation of swept-wing vortices using nonlinear parabolized stability equations," Journal of Fluid Mechanics, Vol. 405, 2000, pp. 325–349.

[2] Gao, B., Park, D. H., and Park, S. O., "Stability analysis of a boundary layer over a hump using parabolized stability equations," Fluid Dynamics Research, Vol. 43, No. 5, 2011, p. 055503.

[3] Franco, J., Hein, S., and Valero, E., "On the influence of two-dimensional hump roughness on laminar–turbulent transition," Physics of Fluids, Vol. 32, No. 3, 2020, p. 034102.

[4] Hein, S., "Linear and nonlinear nonlocal instability analyses for two-dimensional laminar separation bubbles," Laminar-Turbulent Transition, Springer, 2000, pp. 681–686.

[5] Theofilis, V., Hein, S., and Dallmann, U., "On the origins of unsteadiness and three-dimensionality in a laminar separation bubble," Philosophical Transactions of the Royal Society of London. Series A: Mathematical, Physical and Engineering Sciences, Vol. 358, No. 1777, 2000, pp. 3229–3246.

[6] Tocci, F., Franco, J. A., Hein, S., Chauvat, G., and Hanifi, A., "The Effect of 2-D Surface Irregularities on Laminar-Turbulent Transition: A Comparison of Numerical Methodologies," STAB/DGLR Symposium, Springer, 2020, pp. 246–256.

[7] Park, D., and Park, S. O., "Linear and non-linear stability analysis of incompressible boundary layer over a two-dimensional hump," Computers & Fluids, Vol. 73, 2013, pp. 80–96. https://doi.org/https://doi.org/10.1016/j.compfluid.2012.12.007, URL https://www.sciencedirect.com/science/article/pii/S0045793012004586.

[8] Wörner, A., Rist, U., and Wagner, S., "Humps/steps influence on stability characteristics of two-dimensional laminar boundary layer," AIAA Journal, Vol. 41, No. 2, 2003, pp. 192–197.

[9] Park, D., and Oh, S., "Effect of shape of two-dimensional smooth hump on boundary layer instability," International Journal of Aeronautical and Space Sciences, Vol. 21, No. 4, 2020, pp. 906–923.

[10] Cooke, E. E., Mughal, S., Sherwin, S., Ashworth, R., and Rolston, S., "Destabilisation of stationary and travelling crossflow disturbances due to forward and backward facing steps over a swept wing," IUTAM Laminar-Turbulent Transition, edited by S. Sherwin, P. Schmid, and X. Wu, Springer International Publishing, Cham, 2022, pp. 713–723.

[11] Casacuberta, J., Hickel, S., and Kotsonis, M., "Mechanisms of interaction between stationary crossflow instabilities and forward-facing steps," AIAA Scitech 2021 Forum, 2023, p. 0854.

[12] Rius-Vidales, A. F., and Kotsonis, M., "Impact of a forward-facing step on the development of crossflow instability," Journal of Fluid Mechanics, Vol. 924, 2021.

[13] Serpieri, J., "Cross-Flow Instability: Flow diagnostics and control of swept wing boundary layers," PhD Thesis, Delft University of Technology, 2018.

[14] COMSOL Multiphysics® v. 5.6 user guide, COMSOL AB, 2022.

[15] Bertolotti, F. P., Herbert, T., and Spalart, P., "Linear and nonlinear stability of the Blasius boundary layer," Journal of Fluid Mechanics, Vol. 242, 1992, pp. 441–474.

[16] Herbert, T., "Parabolized stability equations," Annual Review of Fluid Mechanics, Vol. 29, No. 1, 1997, pp. 245–283.

[17] Westerbeek, S., "Development of a nonlinear parabolized stability equation (NPSE) analysis tool for spanwise invariant boundary layers," MSc Thesis, Delft University of Technology, 2020.

[18] Zoppini, G., Westerbeek, S., Ragni, D., and Kotsonis, M., "Receptivity of crossflow instability to discrete roughness amplitude and location," Journal of Fluid Mechanics, Vol. 939, 2022.

[19] Franco, J. A., and Hein, S. J., "Adaptive Harmonic Linearized Navier-Stokes equations used for boundary layer instability analysis in the presence of large streamwise gradients," 2018 AIAA Aerospace Sciences Meeting, 2018, p. 1548.

[20] Hein, S., Bertolotti, F. P., Simen, M., Hanifi, A., and Henningson, D., "Linear nonlocal instability analysis - the linear NOLOT code," Internal report IB 223-94, Vol. A56, 1995.

[21] Westerbeek, S., and Kotsonis, M., "An efficient harmonic Navier-Stokes solver for non-linear stability problems in complex domains [Manuscript in preparation]," Journal of Computational Physics, Vol. -, No. -, 2023, pp. –.

[22] Appel, T., "Boundary layer instabilities due to surface irregularities: a harmonic Navier-Stokes approach," PhD Thesis, Imperial College London, 2020.

[23] Streett, C., and Macaraeg, M., "Spectral multi-domain for large-scale fluid dynamic simulations," Applied Numerical Mathematics, Vol. 6, No. 1-2, 1989, pp. 123–139.

[24] Streett, C., "Direct harmonic linear Navier-Stokes methods for efficient simulation of wave packets," 36th AIAA Aerospace Sciences Meeting and Exhibit, 1998, p. 784.

[25] Joslin, R. D., Validation of three-dimensional incompressible spatial direct numerical simulation code: A comparison with linear stability and parabolic stability equation theories for boundary-layer transition on a flat plate, Vol. 3205, National Aeronautics and Space Administration, Office of Management, 1992.

[26] Lanzerstorfer, D., and Kuhlmann, H. C., "Three-dimensional instability of the flow over a forward-facing step," Journal of fluid mechanics, Vol. 695, 2012, pp. 390–404.

[27] Casacuberta, J., Hickel, S., and Kotsonis, M., "Steady and unsteady effects in laminar-turbulent transition due to supercritical forward-facing steps in crossflow [Manuscript in preparation]," , 2023.

Appendix

HNS Matrix Contents

$$[A]\hat{\mathbf{q}}_{m,n} + [B]\omega\hat{\mathbf{q}}_{m,n} + [C]\beta\hat{\mathbf{q}}_{m,n} + [D]\beta^2\hat{\mathbf{q}}_{m,n} + [E]\frac{\partial\hat{\mathbf{q}}_{m,n}}{\partial\xi} + [F]\frac{\partial^2\hat{\mathbf{q}}_{m,n}}{\partial\xi^2} = \mathbf{r}_{m,n},$$

with

$$A = \begin{bmatrix} A_1 + \frac{\partial U}{\partial x} & \frac{\partial U}{\partial y} & 0 & \eta_x D_1 \\ \frac{\partial V}{\partial x} & A_1 + \frac{\partial V}{\partial y} & 0 & \eta_y D_1 \\ \frac{\partial W}{\partial x} & \frac{\partial W}{\partial y} & A_1 & 0 \\ \eta_x D_1 & \eta_y D_1 & 0 & 0 \end{bmatrix},$$

$$B = \begin{bmatrix} -i & 0 & 0 & 0 \\ 0 & -i & 0 & 0 \\ 0 & 0 & -i & 0 \\ 0 & 0 & 0 & 0 \end{bmatrix},$$

$$C = \begin{bmatrix} iW & 0 & 0 & 0 \\ 0 & iW & 0 & 0 \\ 0 & 0 & iW & i \\ 0 & 0 & i & 0 \end{bmatrix},$$

$$D = \begin{bmatrix} \frac{1}{Re} & 0 & 0 & 0 \\ 0 & \frac{1}{Re} & 0 & 0 \\ 0 & 0 & \frac{1}{Re} & 0 \\ 0 & 0 & 0 & 0 \end{bmatrix},$$

$$E = \begin{bmatrix} E_1 & 0 & 0 & \xi_x \\ 0 & E_1 & 0 & \xi_y \\ 0 & 0 & E_1 & 0 \\ \xi_x & \xi_y & 0 & 0 \end{bmatrix}$$

$$F = \begin{bmatrix} -\frac{1}{Re}\xi_x^2 - \frac{1}{Re}\xi_y^2 & 0 & 0 & 0 \\ 0 & -\frac{1}{Re}\xi_x^2 - \frac{1}{Re}\xi_y^2 & 0 & 0 \\ 0 & 0 & -\frac{1}{Re}\xi_x^2 - \frac{1}{Re}\xi_y^2 & 0 \\ 0 & 0 & 0 & 0 \end{bmatrix}$$

$$\mathbf{r} = \begin{bmatrix} -\hat{u}\frac{\partial\hat{u}}{\partial\xi}\xi_x - \hat{u}\frac{\partial\hat{u}}{\partial\eta}\eta_x - \hat{v}\frac{\partial\hat{u}}{\partial\xi}\xi_y - \hat{v}\frac{\partial\hat{u}}{\partial\eta}\eta_y - i\beta\hat{u}\hat{w} \\ -\hat{u}\frac{\partial\hat{v}}{\partial\xi}\xi_x - \hat{u}\frac{\partial\hat{v}}{\partial\eta}\eta_x - \hat{v}\frac{\partial\hat{v}}{\partial\xi}\xi_y - \hat{v}\frac{\partial\hat{v}}{\partial\eta}\eta_y - i\beta\hat{v}\hat{w} \\ -\hat{u}\frac{\partial\hat{w}}{\partial\xi}\xi_x - \hat{u}\frac{\partial\hat{w}}{\partial\eta}\eta_x - \hat{v}\frac{\partial\hat{w}}{\partial\xi}\xi_y - \hat{v}\frac{\partial\hat{w}}{\partial\eta}\eta_y - i\beta\hat{w}^2 \\ \\ 0 \end{bmatrix},$$

and

$$A_1 = U\eta_x D_1 + V\eta_y D_1 - \frac{1}{Re}\left(\eta_x^2 D_2 + \eta_{xx} D_1 + \eta_y^2 D_2 + \eta_{yy} D_1\right),$$

$$E_1 = U\xi_x + V\xi_y - \frac{1}{Re}\xi_{xx} - \frac{1}{Re}2\eta_x\xi_x\frac{\partial}{\partial\eta} - \frac{1}{Re}2\eta_y\xi_y\frac{\partial}{\partial\eta} - \frac{1}{Re}\xi_{yy},$$

where D_1 and D_2 are first-order and second-order wall-normal derivative operators respectively.

NPSE Matrix Contents

$$\mathbb{L}\hat{\mathbf{q}}_{m,n} + \mathbb{M}\frac{\partial \hat{\mathbf{q}}_{m,n}}{\partial \xi} + \mathbb{N}\frac{\partial \alpha_{m,n}}{\partial \xi}\hat{\mathbf{q}}_{m,n} = \mathbf{r}_{m,n}, \tag{9}$$

with

$$\mathbb{L} = \begin{bmatrix} L + \frac{\partial U}{\partial x} & \frac{\partial U}{\partial y} & 0 & i\alpha\xi_x + \eta_x D_1 \\ \frac{\partial V}{\partial x} & L + \frac{\partial V}{\partial y} & 0 & \eta_y D_1 + i\alpha\xi_y \\ \frac{\partial W}{\partial x} & \frac{\partial W}{\partial y} & L & i\beta \\ i\alpha\xi_x + \eta_x D_1 & i\alpha\xi_y + \eta_y D_1 & i\beta & 0 \end{bmatrix},$$

$$\mathbb{M} = \begin{bmatrix} M & 0 & 0 & \xi_x \\ 0 & M & 0 & \xi_y \\ 0 & 0 & M & 0 \\ \xi_x & \xi_y & 0 & 0 \end{bmatrix},$$

$$\mathbb{N} = \begin{bmatrix} -\frac{i}{Re}(\xi_x^2 + \xi_y^2) & 0 & 0 & 0 \\ 0 & -\frac{i}{Re}(\xi_x^2 + \xi_y^2) & 0 & 0 \\ 0 & 0 & -\frac{i}{Re}(\xi_x^2 + \xi_y^2) & 0 \\ 0 & 0 & 0 & 0 \end{bmatrix},$$

$$\mathbf{r} = \begin{bmatrix} -\hat{u}\frac{\partial \hat{u}}{\partial \xi}\xi_x - \hat{u}\frac{\partial \hat{u}}{\partial \eta}\eta_x - \hat{v}\frac{\partial \hat{u}}{\partial \xi}\xi_y - \hat{v}\frac{\partial \hat{u}}{\partial \eta}\eta_y - i\beta\hat{u}\hat{w} \\ -\hat{u}\frac{\partial \hat{v}}{\partial \xi}\xi_x - \hat{u}\frac{\partial \hat{v}}{\partial \eta}\eta_x - \hat{v}\frac{\partial \hat{v}}{\partial \xi}\xi_y - \hat{v}\frac{\partial \hat{v}}{\partial \eta}\eta_y - i\beta v\hat{w} \\ -\hat{u}\frac{\partial \hat{w}}{\partial \xi}\xi_x - \hat{u}\frac{\partial \hat{w}}{\partial \eta}\eta_x - \hat{v}\frac{\partial \hat{w}}{\partial \xi}\xi_y - \hat{v}\frac{\partial \hat{w}}{\partial \eta}\eta_y - i\beta\hat{w}^2 \\ 0 \end{bmatrix},$$

where

$$\begin{aligned} L = {} & -i\omega + iU\alpha\xi_x + U\eta_x D_1 + i\alpha V\xi_y + V\eta_y D_1 \\ & + i\beta W + \frac{1}{Re}(\alpha^2(\xi_x^2 + \xi_y^2) + \beta^2) - \frac{1}{Re}(\eta_x^2 + \eta_y^2)D_2 \\ & - \frac{1}{Re}2i\alpha(\eta_y\xi_y + \eta_x\xi_x)D_1 - \frac{1}{Re}i\alpha(\xi_{yy} + \xi_{xx}) \\ & - \frac{1}{Re}(\eta_{xx} + \eta_{yy})D_1, \end{aligned} \tag{10a}$$

and

$$\begin{aligned} M = {} & U\xi_x + V\xi_y - \frac{2i\alpha}{Re}(\xi_x^2 + \xi_y^2) - (\xi_{xx} + \xi_{yy})\frac{1}{Re} \\ & - \frac{2(\eta_y\xi_y + \eta_x\xi_x)}{Re}D_1, \end{aligned} \tag{11a}$$

where D_1 and D_2 are first-order and second-order wall-normal derivative operators respectively.

VII. Base Flows

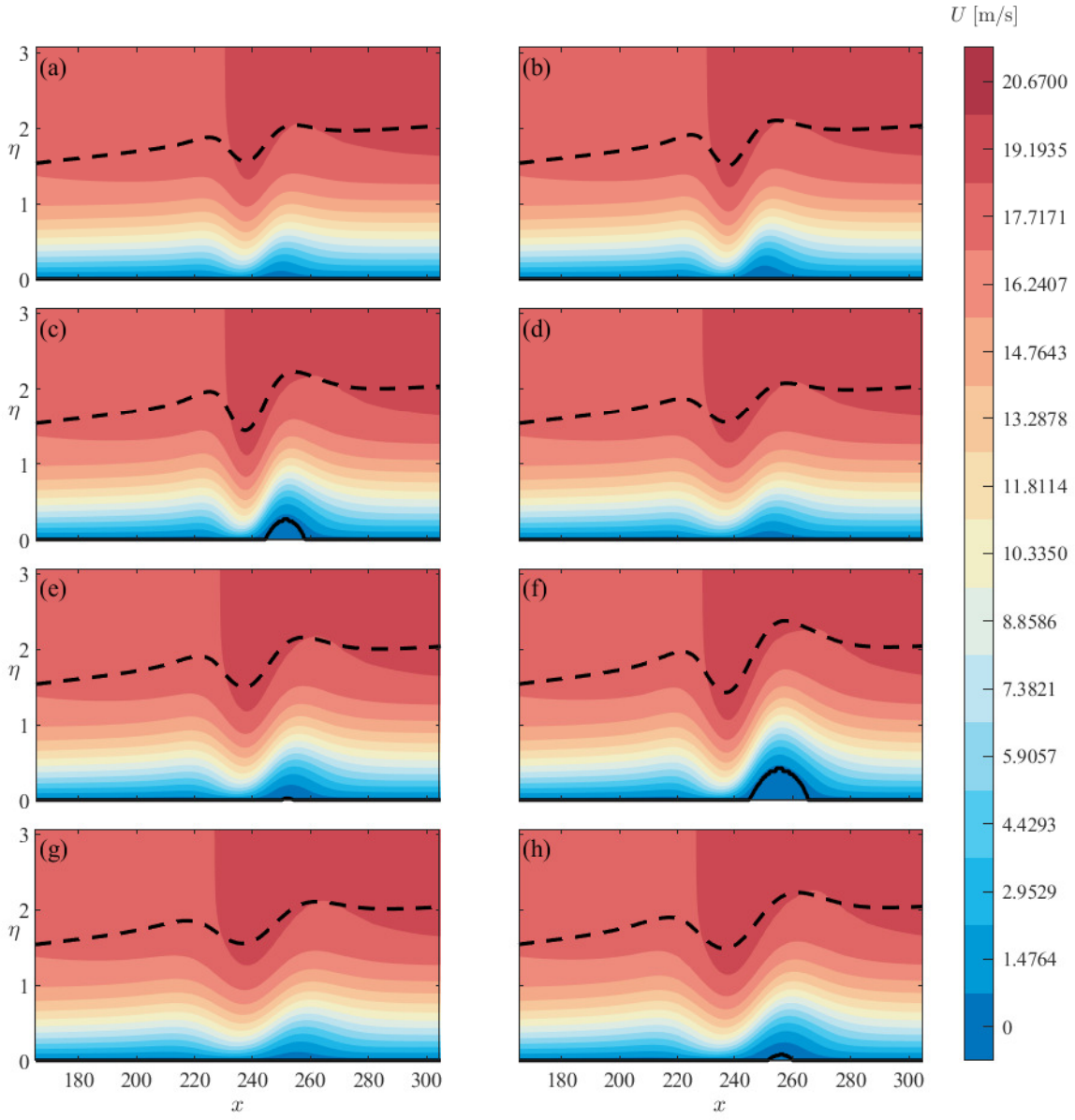

Fig. 7 Streamwise velocity xy plane contours for cases (a) B1, (b) B2, (c) B3, (d) C2, (e) C3, (f) C4, (g) D3 and (h) D4. Solid line marks reverse flow regions and the dashed line is the local δ_{99}.

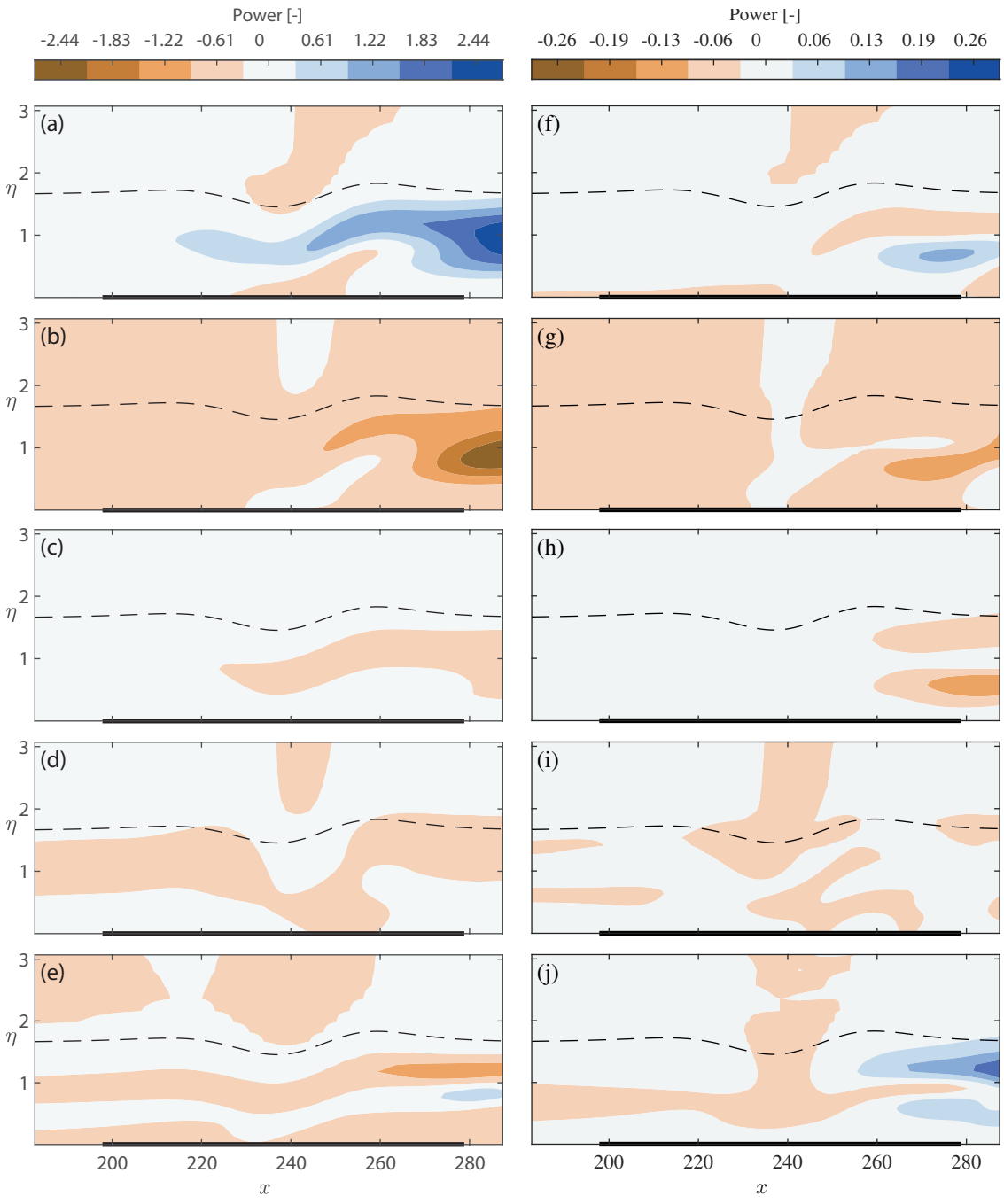

Fig. 8 Energy budget analysis around the wall deformation for case D3 for the primary mode (left) and second harmonic (right) showing the effect of production (a,f), transport (b,g), viscous forces (c,h), pressure work (d,i) and nonlinear terms (e,j). The dashed line indicates the streamline originating from δ_{99} at the inflow and the black bar indicates the location of the protuberance